

Tuneable and free-form planar optics

Pascal Berto^{1,2}, Laurent Philippet¹, Johann Osmond¹, Chang Liu^{2,3}, Adeel Afridi¹, Marc Montagut Marques¹, Bernat Molero Agudo¹, Gilles Tessier^{2,3}, Romain Quidant^{1,4}

¹ICFO-Institut de Ciències Fotòniques, The Barcelona Institute of Science and Technology, 08860 Castelldefels (Barcelona), Spain.

²Sorbonne Paris Cité, Université Paris Descartes, Neurophotonics Laboratory, CNRS UMR 8250, 45 Rue des Saints Pères, F-75006 Paris, France.

³Sorbonne Université, Institut de la Vision, 17 rue Moreau, 75012, Paris, France.

⁴ICREA- Institució Catalana de Recerca i Estudis Avançats, 08010 Barcelona, Spain.

The advent of spatial control over the phase and amplitude of light waves has profoundly transformed photonics, enabling major advances from imaging and information technology to biomedical optics. Here, we propose a novel approach to deterministic phase-front shaping through a planar thermo-optical module using designed microheaters to locally shape the refractive index distribution. When combined with a genetic algorithm optimisation, this *SmartLens* can produce free-form optical wavefront modifications. Individually or in arrays, it can generate complex functions based on either pure, or a combination of, Zernike polynomials, including lenses or aberration correctors of electrically-tuneable magnitude. This simple and compact concept complements the existing optical shaping toolbox by offering low chromatic aberrations, polarisation-insensitive and transmission-mode components which can be readily integrated into existing optical systems.

Introduction - Among the different phase modulation approaches, Spatial Light Modulators (SLMs) have quickly become the gold standard for dynamically controlling the spatial phase profile of wavefronts. Nowadays, million-pixels Liquid Crystal SLMs (LC-SLMs) are the tool of choice for high-resolution versatile light shaping^{1,2}. However, LC-SLMs are inherently polarisation-sensitive and only allow discrete, wavelength-dependent phase manipulations over a few radians. This limits their range of applicability, in particular for imaging. Owing to their sub-100 μ s response times, deformable mirrors have greatly contributed to the fields of astronomy, ophthalmology and microscopy³, where their limited number of achromatic actuators efficiently corrects low-order aberrations. However, besides their manufacturing complexity and price, their reflective operation mode forbids several applications such as endoscopic imaging.

As a result of their compact design, cost efficiency, and their ability to work in transmission over a broad wavelength range, tuneable lenses have found many research and consumer applications. Most existing technologies are based on polymer or liquid surface (or interface) deformations. While commercial devices using electrowetting^{4,5} or pressure regulation⁶ typically have centimetre dimensions, extensive efforts have been recently made to develop microscale tuneable lenses by using electro-mechanic⁷⁻⁹, thermo-pneumatic^{10,11}, electromagnetic^{12,13}, optical¹⁴ and thermal^{15,16} actuators, or by using stimuli-responsive hydrogels¹⁷. At the microscale, the vast majority of devices are still limited by the few degrees of freedom available to mechanical interface deformations, essentially restricting the shaping to spherical wavefronts, i.e. lenses of variable optical power, and freeform optical elements with high degree of freedom are still beyond reach.

However, mechanical deformations of the optics are not the only way to control the optical phase: one can also change the refractive index. Among the few parameters that can influence the dielectric permittivity (e.g. pressure, electric or magnetic fields), temperature is probably the easiest to manipulate. The permittivity and refractive index of most materials are indeed temperature-

dependent ($\Delta n(T) \approx [dn/dT] \Delta T$ in the linear approximation, with $dn/dT \approx 10^{-4}$ - 10^{-5} in dielectrics¹⁸). This thermo-optical phenomenon (responsible for mirages) is used in a wide range of photothermal techniques including photo- or thermoreflectance^{19,20}, absorption spectroscopies^{21,22} or nano-object detection^{23,24} to cite a few. Recently, we demonstrated that heating plasmonic nanoparticle arrays with IR light can modify the refractive index of the surrounding water to generate microlenses²⁵. However, optical stimulation is not the most practical choice for industrial, domestic, or even laboratory applications: historically, electrical control has always prevailed whenever it was available.

Here, we propose a new paradigm-shift to accurately engineer optical wavefronts by exploiting electrically-induced thermal phase-shifts at the microscale. By using an optimised design, resulting from a genetic algorithm, we demonstrate broadband, polarisation-insensitive electrical components which can apply a predetermined, continuous local wavefront shaping with unprecedented degrees of freedom. We show that this device, coined as *SmartLens*, can efficiently generate elementary Zernike polynomial functions and therefore dynamically create a variety of optical functions. When arranged in an array, it can control, correct or refocus various regions of polychromatic wavefronts or images, as illustrated in a simple but powerful example based on a tuneable and broadband microlens array.

Figure 1 describes the overall concept of the technology. A theoretical model, coupled to a genetic algorithm, enables the precise design of a resistive microwire (Fig. 1(a)). Following microfabrication (see Fig. 1(b)), the device is electrically powered to deliver, through Joule effect, the pre-determined temperature landscape $\Delta T(x, y, z)$ into a thermo-responsive polymer matrix (see Fig. 1(c)). Due to the temperature dependence of its refractive index, the polymer experiences a local refractive index modulation (Fig. 1(d)) that precisely shapes the incoming light wavefront with the pre-determined pattern that was fed into the genetic algorithm. To validate our approach experimentally, we designed and characterised several SmartLenses able to create a wide range of wavefront modifications and demonstrated their phase amplitude tunability. In contrast to LC-SLMs or LC microlenses^{26–28}, the SmartLens is polarisation-insensitive since it involves thermally-induced non-birefringent refractive index modulation. As it operates in a refractive rather than diffractive regime, it can also be used over a broad wavelength range. Furthermore, unlike deformable mirrors, SmartLens elements can work either in transmission or reflection modes and do not involve any mechanical movement. Since their fabrication involves a simple process which is compatible with large-scale production, these cost-efficient devices can be scaled-down to micrometre sizes and integrated into multi-element devices (see Fig. 1(b)).

Electro-thermo-optical model – For a resistor generating a Joule power distribution P_0 , an efficient way to calculate the induced temperature rise field ΔT involves a convolution by the thermal Green's function^{29,30} $G_T = \frac{1}{4\pi\kappa r}$. Here, G_T corresponds to the steady-state temperature distribution induced by a point-like source of heat in a homogenous medium with thermal conductivity κ and :

$$\Delta T = P_0 \otimes G_T$$

As discussed above, this temperature field ΔT changes the refractive index through the thermo-optic coefficient dn/dT . An incoming plane wave passing through the PDMS layer will accumulate an Optical Path Difference (OPD) δ during its path through the temperature and refractive index fields, which can be obtained in a similar way using the following equation^{29,30}:

$$\delta = P \otimes G_\delta$$

where $G_\delta = \frac{[dn/dT]}{4\pi\kappa} \cdot \sinh^{-1}(h/r)$, is the Green's function for the OPD, i.e. the OPD distribution generated by a point-like heat source in a medium of thickness h . As illustrated in Fig. 2(a)-(c), this process allows a direct and fast calculation of the wavefront generated by a given resistor through a precise estimation of the dissipated power P which takes into account temperature-dependent resistivity (see Methods). This entire calculation takes less than 1 s where a Finite Element Method (e.g. COMSOL MULTIPHYSICS) calculation would typically require 1 h.

However, the desired OPD can only be reached by solving the inverse problem. In Fig. 2(d) and in the Methods section, we present a genetic algorithm-based method to determine the optimal resistor design leading to a targeted wavefront shape.

Experimental validation of the model - To validate this model, we designed and fabricated a SmartLens element based on a microfabricated gold wire (see Methods) with a simple geometry: a 200- μm diameter spiral heater with 9 regularly spaced loops of constant width w . This structure was coated with an $h = 1$ mm thick PDMS layer, a thermo-responsive polymer chosen for its high transparency in the visible region, its thermal stability at high temperature³¹, and because it exhibits relatively large refractive index variations with temperature³² ($[dn/dT] = -4.5 \cdot 10^{-4} \text{ K}^{-1}$). Although the temperature rise (typ. 50 K) used here induces small refractive index changes (typ. 10^{-2}), beam propagation through hundreds of micrometres of PDMS results in significant OPDs, of the order of several micrometres.

We experimentally measured OPD using a shearing interferometry-based wavefront sensor (SID4, Phasics S.A.) under a custom-built microscope ($\times 10$, NA = 0.25). The spiral-shaped resistor was illuminated using a $\lambda = 542$ nm LED, through a Köhler illuminator set at low numerical aperture in order to increase the spatial coherence (see Supplementary 2). To extract the thermal contribution to the OPD, we subtracted the wavefront measured while the device was off ($V = 0$) from the wavefront measured when heating the device ($V \neq 0$). In this way, the static aberrations of the microscope and the SmartLens are both removed (see Fig. S12(a)). Figures S2(b) and (d) show a spectacular agreement between experimental and simulated OPD maps for different applied voltages, thus validating our electro-thermo-optical wavefront modelling. Interestingly, from the thermal OPD measurement, one can extract the experimental temperature map in the plane of the resistor, with micrometre resolution^{29,30} (see Fig. S2(c) and (d)). This is obtained by (i) deconvolving the thermal OPD map by the Green's function G_δ to retrieve the heat power map P , and then (ii) convolving this retrieved power map P by the thermal Green function G_T . Experimental and simulated temperature maps are in good agreement, and are useful to ensure that the PDMS damage ceiling temperature³¹ ($T = 250$ °C) is not reached.

Deterministic wavefront control by thermal engineering - To illustrate the possibilities of achieving free-form dynamic optical systems to create complex optical wavefronts, we chose to realise a set of three different elementary optical functions: a lens, a phase piston and an axicon lens with tuneable amplitudes. To illustrate the broad possibilities of this concept to emulate or correct various optical designs, we also show that non-rotationally symmetrical Zernike polynomials can be generated, including, but not limited to, astigmatism. A broad range of wavefronts should therefore be accessible.

By combining the above electro-thermo-optical modelling with genetic algorithm optimisation, the inverse problem can be solved in order to determine the optimal resistor geometry leading to a desired wavefront shape (see Fig. 2(d)). Briefly, genetic algorithms are stochastic optimisation methods inspired by the laws of natural selection and genetics^{33,34}: at each step, *crossover* and *mutation* (random processes which avert convergence towards local minima) are used to produce

populations of electrical designs, from which the best are selected using a merit function. Since most microfabrication processes impose a constant thickness h_g of the wire throughout the chip, here $h_g = 50$ nm, the variables are therefore the number N , radii r_i , and widths $w(r_i)$ of the resistive wire loops (see Fig. 2(a)). After typically 60 iterations, corresponding to optimisation times of the order of 30 min, we obtained designs approaching the targeted wavefronts (see Methods).

Figure 3 displays experimental results obtained from a set of resistor designs optimised for four different desired wavefronts. In each case, we show an optical reflection image of the fabricated SmartLens element, along with the corresponding experimental temperature and OPD maps. We also provide a comparison between calculated and experimental OPD profiles for different voltages as well as a 3D representation of the experimental wavefront.

The design of Fig. 3(a) produces a diverging parabolic lens as confirmed by Zernike decompositions (see Fig 3(e)). Figure 3(b) demonstrates a flat phase piston for this polymer thickness. However, as shown in supplementary S3, a thinner polymer can lead the same design to behave as a converging lens. The design of Fig. 3(c) produces a conical wavefront and therefore behaves like an inverted axicon providing a simple way to obtain a tuneable annular beam. The setup described in Fig. 4(b) transmits a Gaussian beam when the device is switched off (0 V), and an annular beam with a voltage-controlled diameter when switched on (see Fig. 4(a)). This implementation has potential applications in several fields, ranging from optical trapping to plasmonics. Used in the configuration of Fig. 4(c), the same device can produce tuneable Bessel-Gaussian beams, which are extensively used in light-sheet microscopy, micro-manipulation, etc. The interferences produced by refocusing the annular beam has geometrical properties driven by the cone angle. As shown in Figs. 4 (d)-(f), this angle increases with the applied voltage, reducing the axial confinement and lateral extension of the beam, thereby providing an electrically-controlled Bessel-Gaussian beam.

Finally, Figures 3(d)-(f) show that astigmatism, or other Zernike modes can be generated: the method is not limited to wavefronts displaying rotational symmetry. More complex freeform shapes can be generated (as shown in Supplementary S4) provided that i) no wire exceeding the fabrication resolution is involved, and ii) the targeted wavefront does not contain phase gradients steeper than the $\sinh^{-1}(h/r)$ decay of the OPD Green's function, as this would demand negative heat sources (or heat sinks). This condition can be relaxed at the expense of phase range by reducing the PDMS thickness h (see Supplementary S5).

Phase tunability range and response time - For this study, we chose a simple design, consisting of regularly-spaced loops of constant width, and fabricated four spirals of different diameters $D = 10, 50, 200$ and 540 μm (see Fig. 5(a)) which act as tuneable diverging lenses. The experimental OPD profile can then be approximated^{35–37} by a parabola $\delta = f \left(1 - \frac{x^2}{2f^2} \right)$ in order to estimate the focal length f (see Fig. 5(b)). Figure 5(c) shows, for four spiral sizes, the measured focal length (in log scale) depending on the applied voltage V (in Volts). When the SmartLens is off ($V = 0$ V), the device acts as a plane-parallel plate (infinite focal length). Interestingly, the focal length $|f|$ decreases faster with the applied voltage V for smaller heaters, since the radius of curvature of the generated lens is shorter. For instance, the vergence of the 10 μm diameter spiral reaches $f = -110$ μm for $V = 2.1$ V which corresponds to a f-number $|f/D| = 11$. Furthermore, it is noteworthy that the accuracy and precision of the phase, and thus of the focal length, are only limited by the applied voltage accuracy and precision.

To evaluate the response time of the device, we applied a square 0.5 Hz, 0 V-2.5 V modulation. Figure 5(d) shows the measured optical power $P_{OP} = 1/f$ against time, for $D = 50$ μm (blue line) and $D = 200$ μm (red line). From the temporal traces, we extracted the rise time (resp. fall time) by measuring the 10 % to 90 % (resp. 90 % to 10 %) optical power transition time with respect to the steady-state

maximum value. Figure 5(e) represents a semi-log graph of the measured rise times (red circles) and fall times (blue circles) for each SmartLens diameter D . These values are in good agreement with the time scale of the temperature evolution³⁸ (black line) on a surface with a characteristic size D : $\tau = D^2/(4a_s)$, where a_s is the thermal diffusivity of the substrate ($a_s \approx 3.4 \cdot 10^{-7} \text{ m}^2 \cdot \text{s}^{-1}$ for glass). Among the tested spirals, the smallest ones (10 μm diameter) enabled fast response times, around 500 μs .

Broadband spectral operation - Many applications, ranging from microscopy to machine vision, require optical elements capable of operating over a broad wavelength range. However, diffractive optical elements, including LC-SLMs, suffer from strong chromatic aberrations due to abrupt phase jumps ($0-2\pi$). In spite of extensive efforts over the last few years^{39,40}, diffractive dispersion still limits their range of applicability, especially for broadband imaging. Here, we show that SmartLens devices have low dispersion, comparable to that of classical glass lenses since the phase is only modified by a smoothly varying refractive index distribution. To demonstrate these broadband properties, we assessed the longitudinal chromatic aberration of a diverging SmartLens ($D = 200 \mu\text{m}$ – see Fig. 5(a)). To this aim, we measured the focal length using the wavefront sensing setup described above, using six LEDs with different colours. Figure 6(a) shows the wavelength dependence of the measured focal length throughout the visible spectrum, for three different applied voltages (6, 9 and 12 V), showing remarkably constant focal length across the visible spectrum.

In contrast to classical lenses, the chromatic aberrations of a SmartLens does not result directly from refractive index dispersion $n(\lambda)$ but essentially derives from the dispersion of the thermo-optic coefficient $[dn/dT](\lambda)$. To characterise the chromatic aberrations of the SmartLens at a given applied voltage, we introduce the dimensionless parameter $\Delta f/f_0$, where $\Delta f = f(\lambda) - f_0$, stands for the paraxial focal shift related to the focal length f_0 (arbitrarily defined near the centre of the visible spectrum, $\lambda_0 = 542 \text{ nm}$). Table 1 of Supplementary 7 shows that for the three applied voltages $\Delta f/f_0$ remains below 2 % in the 475-631 nm wavelength range and reaches 5.4 % in the violet ($\lambda = 390 \text{ nm}$). We also compare the chromatic aberrations of a SmartLens to the theoretical aberrations of a model diverging thin plano-concave PDMS lens and conclude that a SmartLens performs similarly to a classical bulk lens ($\Delta f/f_0 \approx 1.0 \%$ in the 475-631 nm wavelength range).

Simultaneous multiplane imaging using an array of SmartLenses - Finally, we illustrate the potential of an array of SmartLenses to achieve broadband multiplane imaging. Here, an array of 5x5 thermal microlenses located close to the image plane of a lens enables the simultaneous refocusing of several coloured objects located at various distances from the imaging system. A schematic description of the optical configuration is shown in Fig. 6(c): a zoom lens (Canon EF-S18-55mm), set to a focal length $f = 35 \text{ mm}$, images on a camera five ‘RGB’-coloured objects placed at various distances ($d = 20, 30, 40, 50$ and 60 cm , each with a size calculated to compensate the distance-dependence of magnification). A 5x5 tuneable microlens array ($D = 540 \mu\text{m}$ - see Fig 5(a)) is located 5 mm before the image plane to maximise the refocusing range and minimise cross-talk between microlenses. A x1.5 telescope (omitted in Fig. 6(c) for clarity) matches the size of the microlens array with that of the sensor and conjugates the image in its plane. Each ‘RGB’ label is therefore imaged through an independent smartlens (see Fig. 6(d)).

As shown in Figure 6(d-e) and Video S1, an appropriate voltage can be determined to tune the focal length of the corresponding SmartLens and form a focused image of each object with qualitatively low chromatic aberrations (see quantitative estimation in S7). However, a faint halo, attributed to diffraction by the gold heater is observed. Using transparent conductive materials such as Indium Tin Oxide (ITO) strongly reduces this effect as demonstrated in Supplementary S12. Another important parameter particularly relevant to imaging is transmission loss. While the transmission of the current SmartLens is about 60 % (for a diverging lens-wavefront), values above 90 % are obtained when using

highly transparent conductive materials such as ITO and could be further improved using antireflection coatings. This implementation should find a wide range of applications since it enables different planes of interest to be monitored by simply inserting a SmartLens array, which can be mass-produced at moderate costs, in front of a standard camera. Beyond video surveillance, machine vision, cell phone or camera imaging, the technique has a major potential in microscopy, where the depth of field is extremely limited (see Supplementary S9, and Video S2). Figure 6(b) illustrates the imaging quality allowed by SmartLenses, in the context of microscopy and multiplane refocusing, which can also be appreciated over the entire field of view with a star target, as shown in Supplementary S10. In biology, imaging fast polychromatic processes occurring in various, non-deterministic (x,y,z) positions is essential. For instance, coupling SmartLenses with widefield fluorescence calcium imaging⁴¹ would enable the simultaneous monitoring of fast transient neuron activities at different depths in the brain, although with limited resolution. Interestingly, the proposed strategy is also compatible with endoscopy or miniaturised microscopy since the tuneable array works in transmission and can be easily designed to reach sub-millimetre dimensions. We finally envision that this concept should open new possibilities in all fields where a microlens array is needed, such as spinning disk microscopy⁴², Shack-Hartmann based wavefront-sensing⁴³ or light field imaging⁴⁴.

Discussion and conclusion - The present study illustrates the broad potential of the *SmartLens* concept, as a flexible building block to be incorporated into a wide range of optical instruments in order to boost their performance. As demonstrated above, a broad range of wavefront shapes and Zernike coefficients can be adapted at will by using a genetic algorithm to generate complex (free-form) shapes. One of the most interesting applications of the technology is adaptive optics aberration correction. For instance, in standard microscopes, one single SmartLens in the pupil of the system could be used to dynamically correct spherical aberrations. Several phase masks, corresponding for instance to different Zernike polynomials, could potentially be multiplexed on the same sample by addressing independently each spiral loop, enabling the dynamic correction of most aberrations. As a proof of concept, we restricted the electrical design geometry to a spiral shape. However, it is worth mentioning that much more complex geometries can be implemented to generate tuneable non-centred phase masks, gratings or even engineered diffusers. Another attractive feature of this technology is the use of independent controllable multi-elements arranged in an array. We have presented here an array of 5x5 elements but scaling up the number of elements in order to compete with or surpass standard deformable mirrors (several tens to hundreds of elements) should be possible. As shown by numerical simulations in Supplementary S13, thermal confinement strategies are a promising way to mitigate thermal cross-talk between closely packed heaters. Importantly, SmartLens has a quite low power consumption (below 100 mW) which is highly critical for compatibility with integrated devices. Another advantage is its cost-effectiveness as it requires only few simple fabrication steps that are compatible with standard microelectronics protocols. Concerning the device lifetime, while a dedicated study is out of the scope of this article, high phase stability has been observed over dozens of hours of operation, as long as the applied voltage leads to temperature below the PDMS ceiling temperature.

Acknowledgments - The authors acknowledge financial support from the European Research Council program under grants ERC-CoG QnanoMECA (64790) and ERC-PoC (680898), Fundació Privada Cellex, the CERCA programme and the Spanish Ministry of Economy and Competitiveness, through the “Severo Ochoa” Programme for Centres of Excellence in R&D (SEV-2015-0522) and Région Ile de France (GeneTherm Project– C’Nano IdF– DIM Nano-K 2016-16). The authors also wish to thank José Garcia Guirardo, Josep Canet-Ferrer, Johann Berthelot and Antoine Reserbat-Plantey for their help on the resistor fabrication. We thank Vincenzo D’Ambrosio for his help on data analysis and general discussions on the technology, Philipp Del Hougne for preliminary COMSOL simulations as well as Irene Alda, Renaud Marty and Jon Donner for their preliminary work on SmartLens characterisation. We

also thank Pierre Bohec for stimulating discussions regarding genetic algorithm implementation and Guillaume Baffou for fruitful discussion on the thermal model.

Authors contributions - R.Q. initiated and supervised the project. R.Q. and P.B. conceived the concept. P.B. developed the electro-thermo-optical model and the genetic algorithm optimisation. P.B. and L.P. designed the sample. J.O. and L.P. fabricated the devices. P.B., G.T. and L.P. performed the wavefront sensing experiments and analysed the results. C.L. performed the experiment on Bessel Beam generation. P.B., R.Q., L.P., A.A., M.M.M. and B.M.A. designed and performed the imaging experiment. All authors participated in writing the manuscript.

Methods

Sample Fabrication - The samples were produced in one or two lift-off steps according to the dimensions of the smallest electrode's widths. For dimensions above 2 μm , the lift-off process consisted in UV photolithography with a negative resist (Microchemicals AZ nLOF 2020) on a sodalime wafer. Subsequently Ti (2 nm) / Au (50 nm) were deposited by e-beam and thermal evaporation respectively. Lift-off was completed by removing the resist with acetone. For dimensions below 2 μm a complementary lift-off step was used in addition to the previous one, in order to produce the central parts and the smallest electrodes. Objects with critical dimensions below 2 μm were patterned using this second step. To achieve this resolution, we used electron beam lithography (EBL). On top of the pre-patterned sample we deposited a double layer of PMMA (Microchem 495 A4 + 950 A2) and conductive polymer to avoid charging (Denko, Espacer 300Z). It was then exposed with a Scanning Electron Microscope (FEI InspectF) modified to perform lithography (Raith Elphy plus). The deposition and lift-off processes were identical to those of the first step. Finally, the whole samples were covered with 1 mm of PDMS (Sylgard 184) and a 170 μm thick glass coverslip.

Electro-thermo-optical model - In this section, we provide some details related to the electro-thermo-optical model used to calculate the wavefront shape induced by a given resistor geometry. To this end, the local resistivity, power dissipation, temperature gradient, and refractive index gradient have to be determined. At this stage, we consider a spiral geometry (see Fig. 1(a) and (b)) which is modelled by an assembly of N circular wire-loops (electrical feeds are omitted here, see Figure 2(a)).

Let us consider a circular loop i of radius r_i . For the sake of clarity, here we assume a system with circular geometry. Note, however, that the azimuth θ can be taken into account when generating geometries without axial symmetry, as shown later. The electrical resistance of an infinitesimal wire segment of length $dl = r_i d\theta$ reads:

$$dR(r_i, T) = \frac{\rho(T).dl}{w(r_i).h_g} \quad [1]$$

where h_g stands for the wire thickness, $w(r_i)$ the wire width and $\rho(T)$ the electrical resistivity. The flow of an electric current I through the wire segment locally induces, by Joule effect, a dissipated heat power $dP(r_i, T) = dR(r_i, T).I^2$. For most metals, resistivity increases with temperature, which can be simply described using a linear approximation, $\rho(T) = \rho_0(1 + \alpha\Delta T)$, where α is the temperature coefficient of the resistivity and ρ_0 is the resistivity at room temperature T_0 . By combining the expressions of $dP(r_i, T)$ and $\rho(T)$ with Eq.1, we get the temperature dependence of the Joule power for this small wire segment:

$$dP(r_i) = dP_0(r_i).(1 + \alpha\Delta T) \quad [2]$$

where $dP_0(r_i, T_0) = \frac{\rho(T_0) \cdot dl}{w(r_i) \cdot h_g} I^2$, is the Joule power dissipated when the resistor is at room temperature. From this expression, P_0 can be calculated considering an arbitrary number of loops N with r_i the radius and $w(r_i)$ the width of the i^{th} loop (see Figure 2(a)). As discussed above, the temperature map ΔT can then be calculated through a simple convolution:

$$\Delta T = P_0 \otimes G_T \quad [3]$$

However, as shown by Eq.2, the steady-state deposited power P depends on the local temperature rise ΔT (through the thermal dependence of the resistivity), and the problem is clearly recursive. For better precision, the temperature map ΔT can be used to calculate a more precise Joule power map P , using Eq.2 to account for the temperature dependence of the resistivity. Using equations 2 and 3, this process can be repeated as many times as necessary to converge iteratively towards a more accurate estimation of ΔT and P (see Supplementary 1). Figure 2(b) shows the temperature rise ΔT obtained using this process.

As light passes through this medium, the temperature field ΔT changes the refractive index through the thermo-optic coefficient dn/dT , inducing an Optical Path Difference (OPD) δ which can be directly obtained using the following equation^{29,30}:

$$\delta = P \otimes G_\delta$$

where $G_\delta = \frac{[dn/dT]}{4\pi\kappa} \cdot \sinh^{-1}(h/r)$, is the Green's function for the OPD.

Genetic Algorithm optimisation - Genetic algorithm optimisation was implemented using the *ga* function provided in the MATLAB Global Optimization Toolbox (2016b). For each design optimisation, a dedicated fitness function was defined to estimate, at each step, the agreement between the desired wavefront and the wavefront generated by a given electrical design. The wavefront was calculated by means of the electro-thermo-optical model (see Fig. 2a), by considering the gold resistivity $\rho_0 = 3.1 \cdot 10^{-8} \Omega \cdot m$ at room temperature ($T_0 = 293 \text{ K}$), the temperature coefficient of the gold resistivity $\alpha = 3.4 \cdot 10^{-3} \text{ K}^{-1}$ and the temperature coefficient of the PDMS refractive index³² $[dn/dT] = -4.5 \cdot 10^{-4} \text{ K}^{-1}$. The procedure starts with the creation of a random initial population ($n = 1000$) of design using as variable the number N , radii r_i , and widths $w(r_i)$ of the resistive loops as well as an anisotropy variable A_i in the case of profiles lacking rotational symmetry (e.g. astigmatism). For practical reasons (position of the electrical contacts), only odd values of the number of loops were considered: $N = 1, 3, 5, 7, 9, 11, 13$. As a first step, the algorithm estimated, *via* the fitness function, the merit of each design to determine an optimal number N of loops which was then fixed in the rest of the optimisation procedure (to enable *crossover* between different designs). At each generation (or iteration), the algorithm ranks and selects the 10 best designs and uses them as parents to produce a new population with 200 children designs via *crossover* and *mutation* (constraint dependent). In the overall procedure, linear inequalities constraints as well as lower and upper bounds were added on the radii r_i and widths $w(r_i)$ of the loops to (i) avoid loops superimposition, (ii) define the microlens size ($r_N = 100 \mu m$) and (iii) only consider realistic designs regarding the fabrication methods ($w > 0.5 \mu m$). The voltage was arbitrarily fixed to 6 V. At each generation, fitness calculations were performed in parallel using the MATLAB Parallel Computing Toolbox of on 20 threads (Intel(R) Xeon(R) CPU E5-2630 v4 2.2GHz - RAM: 64Go). Optimisation convergence (fitness average change below 10^{-6}) was typically obtained after 60 generations (Video S3 in the Supplementary information 10).

Wavefront engineering - Genetic algorithm optimization enables the engineering of the wavefront to target a given Zernike polynomial^{45,46}. Zernike polynomials Z_n^m , where n stands for the radial degree and m the azimuthal degree, are a set of orthonormal functions which are widely used in controlling and characterising the aberrations of optical systems. Figure 3(a) shows a resistor designed to

maximise the absolute value of the defocus aberration Z_2^0 over other Zernike aberrations. Here, the design was optimised within a 220 μm diameter pupil (dashed line on the OPD map). A Zernike decomposition of the measured OPD on the first fifteen Zernike modes demonstrates, as expected, a clear predominance of the defocus mode Z_2^0 (see Figure 3(e)). The residual RMS value of other Zernike modes is remarkably low, and mainly due to numerical errors associated with pupil centring for modal projection. Moreover, it is worth mentioning that the negative value of the Z_2^0 coefficient describes a diverging parabolic lens. This is consistent with a higher temperature at the centre and a negative value of dn/dT for PDMS (see Figure 3(a)).

Figure 3(b) shows the design of a “flat” OPD profile, which corresponds to a phase piston. For any pupil radius r_1 smaller than the PDMS thickness h , the optimal design is actually a single loop, as illustrated here for a radius $r_1 = 100 \mu\text{m}$. Note that if h were decreased (or r_1 increased), the same single-loop design would result in a converging lens profile (see Supplementary 3). Here, interestingly, the OPD profiles remain flat for the different applied voltages and can reach values greater than 12 λ . This is a 4-fold improvement as compared to LC-SLM working in reflection, which typically provides a phase modulation range of 3 λ at $\lambda = 550 \text{ nm}$. Figure 3(c) shows the results corresponding to a design optimised to provide a conical wavefront surface $\delta(r) = -\sqrt{r^2/\tan^2\gamma}$, where γ is the apex angle. Again, the amplitude of the conical deformation is controlled by the applied voltage. Such a tuneable negative axicon is interesting in applications where the dynamic control of Bessel beams is crucial, e.g. in light sheet microscopy.

Finally, Figure 3(d) shows that this method is not limited to wavefronts displaying rotational symmetry. More elaborate freeform wavefronts can be created by engineering the spiral wire width not only radially ($w(r_i)$) but also angularly ($w(r_i, \theta)$). Figure 3(d) represents a SmartLens element designed to generate vertical astigmatism $Z_2^2 = R_2^2 \cos(2\theta)$ in a 160 μm diameter pupil. In this case, we fixed the angular periodicity of the wire widths to match the azimuthal degree of the considered Zernike polynomial ($m = 2$) and introduced an anisotropy variable A_i in the fitness function for each wire width: $w(r_i, \theta) = w(r_i)(1 + A_i \cos(m\theta))$. As expected, within the chosen 160 μm diameter pupil, the Zernike decomposition of the measured OPD clearly demonstrates a predominant vertical astigmatism coefficient Z_2^2 (see Figure 3(f)), although a moderate residual amount of defocusing (Z_2^0) is also present. The essential limitation here is the minimum achievable wire width, which is imposed by our current lithography process. Improving resolution to 150 nm or below, or using a larger thermal engineering surface should enable a strong reduction of this effect.

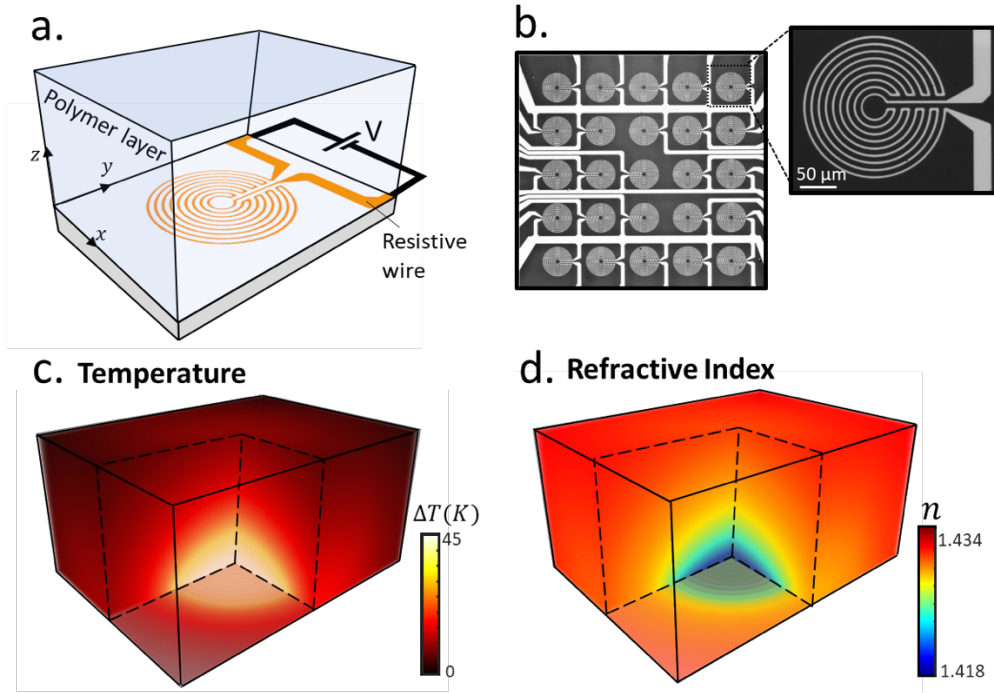
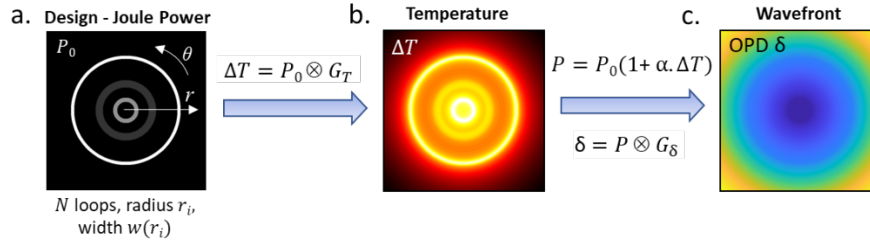


Figure 1 - Principle of the electrically tuneable micro-optic device. Electrically-controlled resistive spirals induce thermal refractive index variation in a thermo-responsive material. **(a)** Schematic of the system. **(b)** Optical reflection images of an array of spirals. **(c)** 3D representation of a typical temperature rise in a thermo-optical polymer inducing **(d)** refractive index changes.

Direct Problem



Inverse Problem

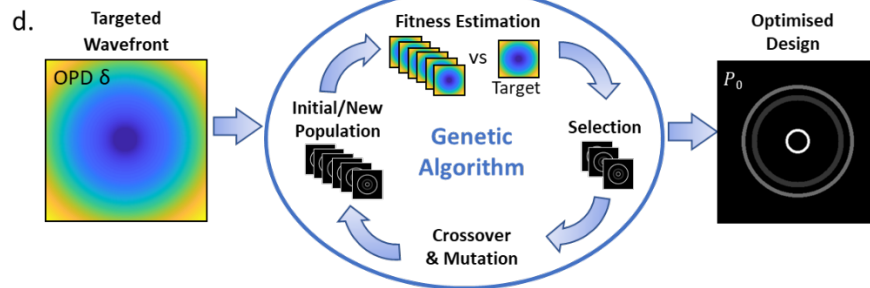


Figure 2 - Modelling and wavefront engineering procedure. The spiral heater is modelled by an assembly of N resistive circular wire-loops of radii r_i and widths $w(r_i)$. An electric current flow induces **(a)** a structured Joule power map P_0 from which **(b)** the temperature map ΔT (at $z = 0$) is calculated by convolution with the thermal Green's function G_T . **(c)** The thermally induced Optical Path Difference (OPD) δ accumulated by an incoming plane wave passing through the PDMS layer is then calculated by a convolution with G_δ , the Green's function for the OPD. **(d)** A genetic algorithm enables to solve the inverse problem in order to precisely determine the electrical design which optimally produces the targeted wavefront.

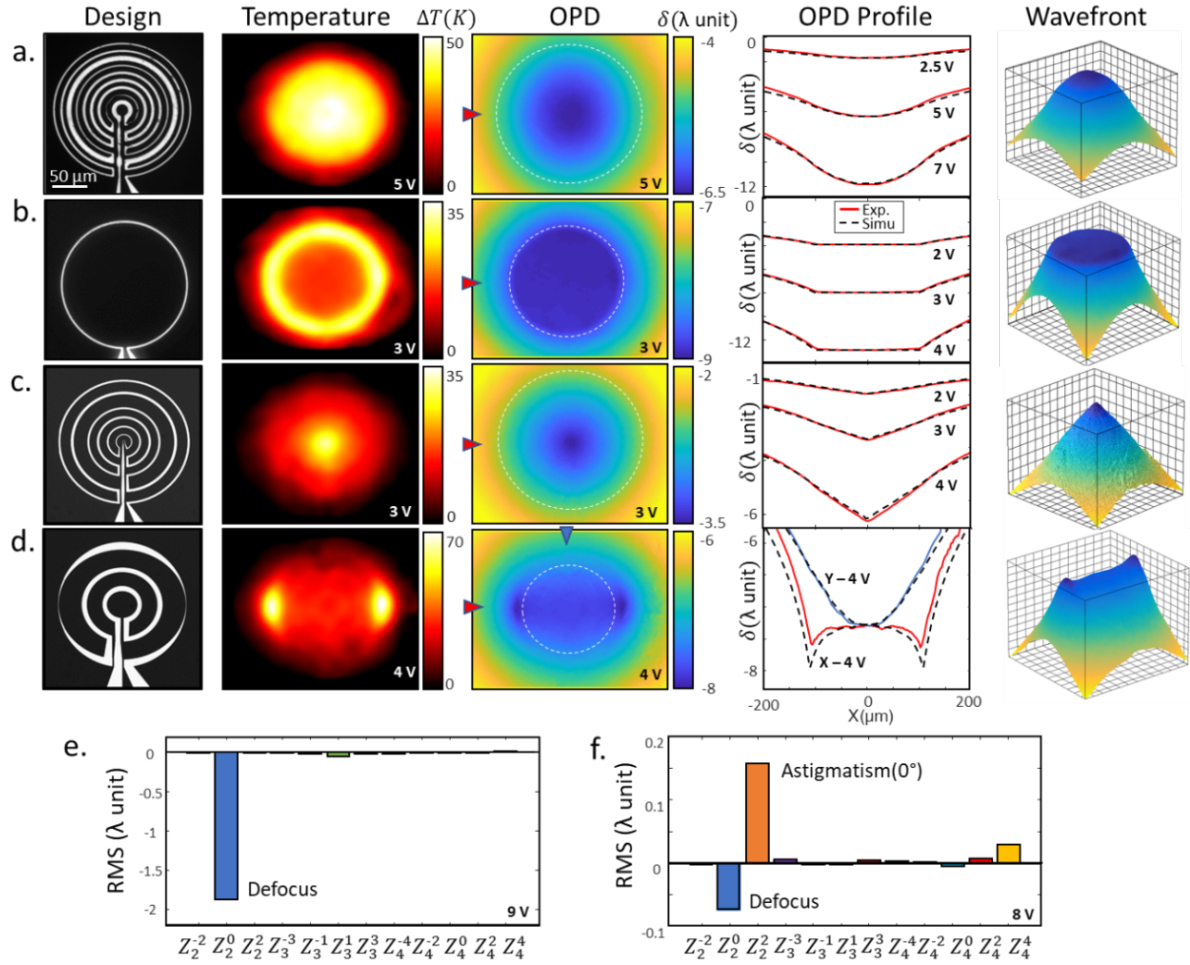


Figure 3 - Wavefront engineering. Experimental results obtained on a set of four spiral geometries optimised for four different wavefronts: **(a)** Defocus (diverging lens). **(b)** Flat profile (piston). **(c)** Conical surface (inverted-axicon). **(d)** Vertical astigmatism. In each case, the optical reflection image, the experimental temperature and OPD maps are shown. On each OPD map, the dashed circle indicates the optimal pupil, which is one of the parameters of the optimisation procedure. A comparison between calculated (dashed line) and experimental (solid line) OPD profiles, for different voltages, or along different directions (indicated by a blue or red arrow on the OPD map) is also provided, as well as 3D representations of the experimental wavefronts (same color scale as the OPD). Zernike decompositions (Z_n^m for $n = 2, 3$ and 4) of the measured OPDs are presented for **(e)** the defocus (shown in (a)) and **(f)** the astigmatism (shown in (d)).

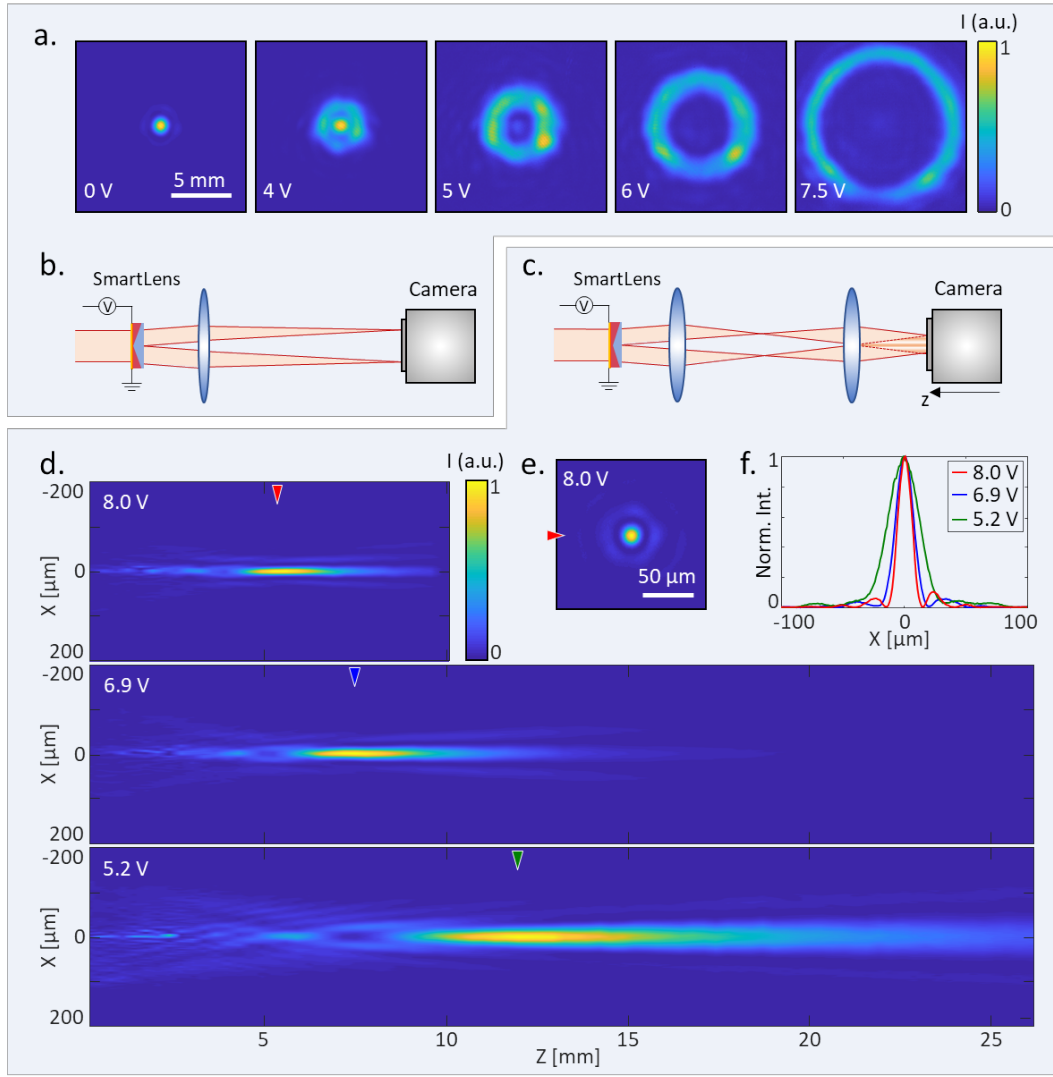


Figure 4 - Generation of tuneable annular and Bessel-Gaussian beams. (a) Intensity profiles of annular beams for different voltages. (b) Simplified setup for annular beam generation. A SmartLens optimized to generate a conical wavefront (inverted axicon – see Fig. 3(c)) is illuminated by a collimated laser. The pupil size ($D = 200 \mu\text{m}$ in the SmartLens plane) is controlled by a pinhole located in a conjugated plane (not shown). The Gaussian beam (for $V = 0$ V) is changed into a ring of controlled diameter for $V \neq 0$ V. In the image space of the (c) simplified setup, ring refocusing produces (d) tuneable Bessel-Gaussian patterns shown in the XZ-plane for different applied voltages (8.0, 6.9 and 5.2 V). The axial extension of the beam increases at lower voltages. (e) XY-section of the Bessel-Gaussian pattern for $V = 8.0$ V, and (f) normalized intensity profiles in the focal plane, showing increased widths for lower voltages.

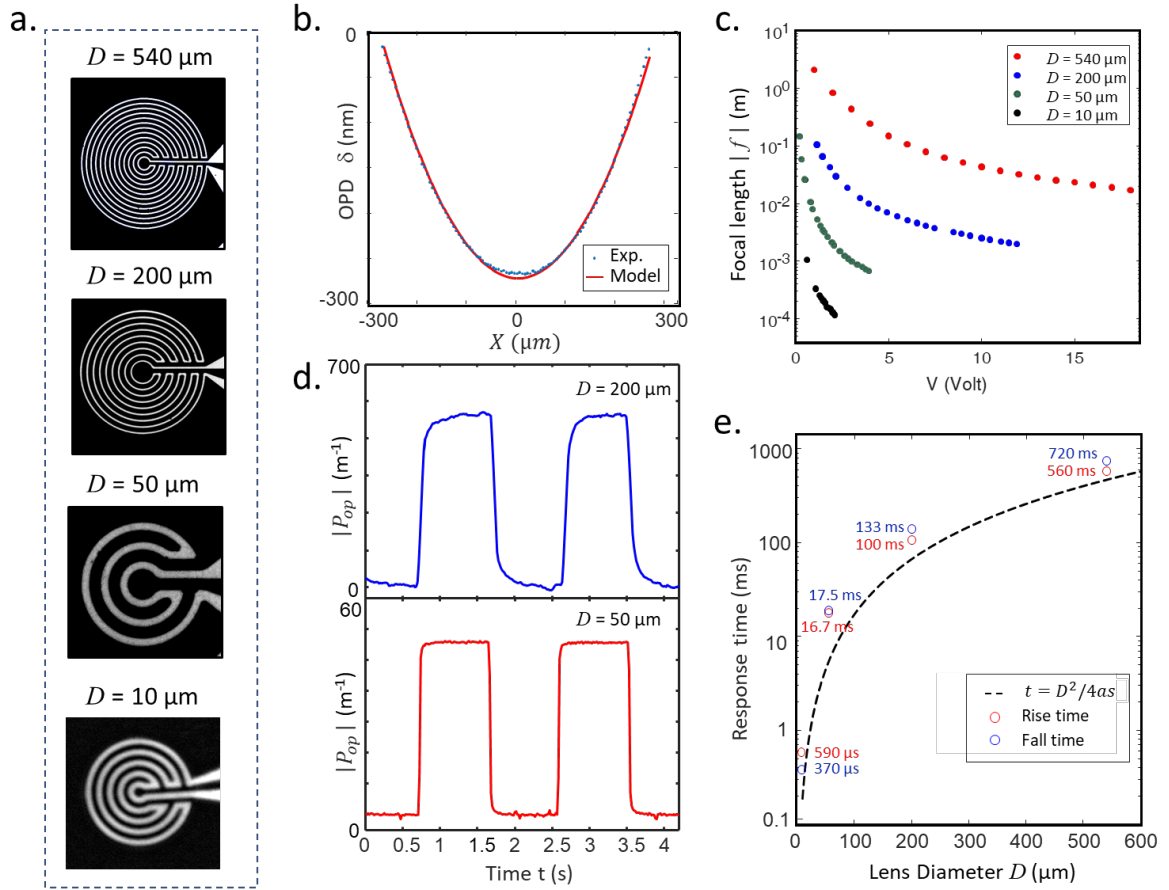


Figure 5 - Tunability ranges and response times for four different spiral sizes. (a) Optical reflection image of four spirals of diameters $D = 10, 50, 200$ and $540\ \mu\text{m}$. (b) Experimental OPD profile (dots). The SmartLens acts as a diverging lens, and the OPD profile is fitted by a parabola (red line) to estimate the focal length f (represented for $D = 540\ \mu\text{m}$, $V = 3\ \text{V}$). (c) Evolution of the focal length (log scale) against applied voltage V for the four spiral sizes. (d) Temporal response to electrical square wave signals (0 V-2.5 V) at 0.5 Hz. (e) Evolution of the response time (in log scale) with spiral diameter D . Experimental estimation of the rise time (red circles) and fall time (blue circles) are in good agreement with the time scale of temperature evolution on a surface of diameter D (dashed line).

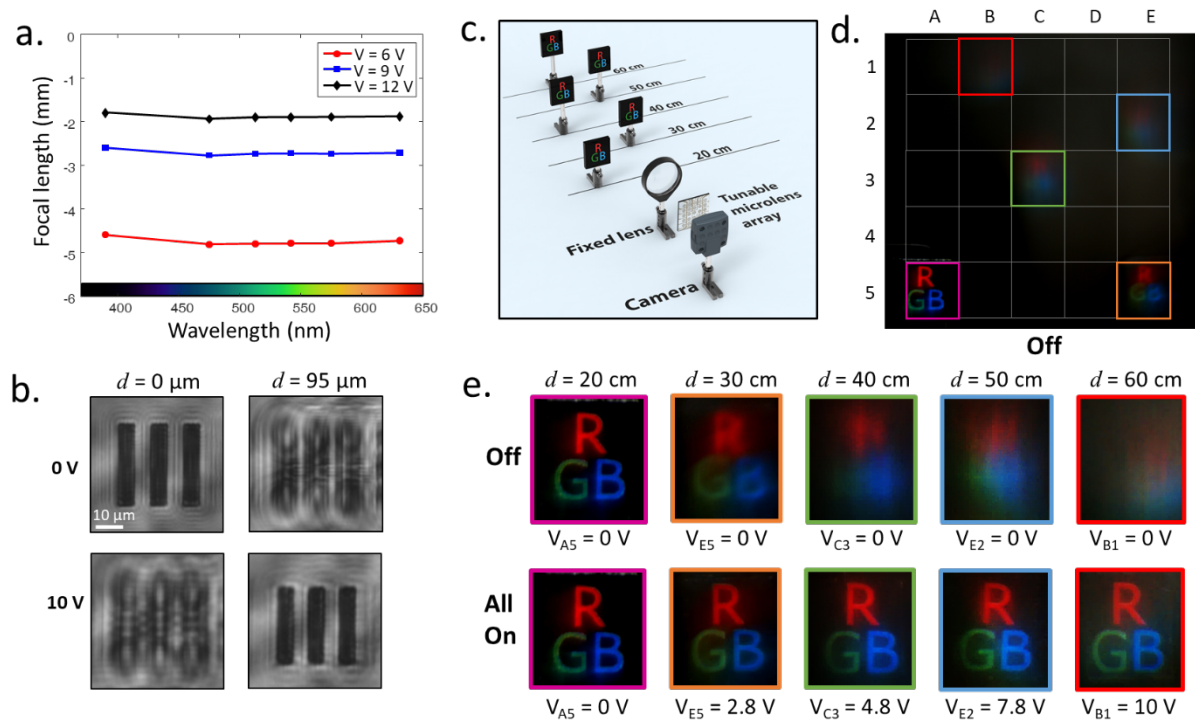


Figure 6 – Broadband multiplane imaging with a Smartlenses array. (a) Axial chromatic aberrations measured for a $D = 200 \mu\text{m}$ diverging lens for voltages 6 (red), 9 (blue) and 12 V (black). (b) Microscopic refocusing of the $6.2 \mu\text{m}$ line (and gap) width element (group 6 element 3) of a 1951 US air force resolution target. (c) Simplified setup for multiplane imaging. A 5×5 Smartlenses array is located 5 mm before the image plane of the lens to simultaneously image five RGB objects placed at various distances. (d) The image is divided in 5×5 regions. When the microlenses are off, only the nearest object (20 cm) is imaged. With adapted voltages, objects located in other planes are brought into focus. (e) Zoom on the different image regions (all on). The min/max values of the lookup table were adapted to compensate the decrease of light collection efficiency with distance.

Data Availability - The data that support the plots within this paper and other finding of this study are available from the corresponding author upon reasonable request.

Correspondence and requests for materials should be addressed to R.Q. or P.B.

References

1. Rubinsztein-Dunlop, H. *et al.* Roadmap on structured light. *J. Opt. (United Kingdom)* **19**, (2017).
2. Maurer, C., Jesacher, A., Bernet, S. & Ritsch-Marte, M. What spatial light modulators can do for optical microscopy. *Laser Photonics Rev.* **5**, 81–101 (2011).
3. Hornbeck, L. J. Deformable-Mirror Spatial Light Modulators. *Spie* **1150**, 1–17 (1989).
4. Berge, B. & Peseux, J. Variable focal lens controlled by an external voltage: An application of electrowetting. *Eur. Phys. J. E* **3**, 159–163 (2000).
5. Kuiper, S. & Hendriks, B. H. W. Variable-focus liquid lens for miniature cameras. *Appl. Phys. Lett.* **85**, 1128–1130 (2004).
6. Ren, H., Fox, D., Anderson, P. A., Wu, B. & Wu, S.-T. Tunable-focus liquid lens controlled using a servo motor. *Opt. Express* **14**, 8031 (2006).
7. Liebetraut, P., Petsch, S., Liebeskind, J. & Zappe, H. Elastomeric lenses with tunable

- astigmatism. *Light Sci. Appl.* **2**, (2013).
8. Beadie, G. *et al.* Tunable polymer lens. *Opt. Express* **16**, 11847 (2008).
 9. Carpi, F., Frediani, G., Turco, S. & De, R. D. Bioinspired tunable lens with muscle-like electroactive elastomers. *Adv. Funct. Mater.* **21**, 4152–4158 (2011).
 10. Zhang, W., Zappe, H. & Seifert, A. Wafer-scale fabricated thermo-pneumatically tunable microlenses. *Light Sci. Appl.* **3**, 0 (2014).
 11. Zhang, D. Y., Lien, V., Berdichevsky, Y., Choi, J. & Lo, Y. H. Fluidic adaptive lens with high focal length tunability. *Appl. Phys. Lett.* **82**, 3171–3172 (2003).
 12. Liebetraut, P., Petsch, S., Mönch, W. & Zappe, H. Tunable solid-body elastomer lenses with electromagnetic actuation. *Appl. Opt.* **50**, 3268 (2011).
 13. Yu, H., Zhou, G., Chau, F. S. & Sinha, S. K. Tunable electromagnetically actuated liquid-filled lens. *Sensors Actuators, A Phys.* **167**, 602–607 (2011).
 14. Xu, S. *et al.* Adaptive liquid lens actuated by photo-polymer. *Opt. Express* **17**, 17590 (2009).
 15. Glebov, A. L., Huang, L., Aoki, S., Lee, M. & Yokouchi, K. Planar hybrid polymer-silica microlenses with tunable beamwidth and focal length. *IEEE Photonics Technol. Lett.* **16**, 1107–1109 (2004).
 16. Angelini, A., Pirani, F., Frascella, F. & Descrovi, E. Reconfigurable elastomeric graded-index optical elements controlled by light. *Light Sci. Appl.* **7**, 1–9 (2018).
 17. Dong, L., Agarwal, A. K., Beebe, D. J. & Jiang, H. Adaptive liquid microlenses activated by stimuli-responsive hydrogels. *Nature* **442**, 551–554 (2006).
 18. Ghosh, G. *Handbook of Thermo-Optic Coefficients of Optical Materials with Applications. Chemistry &* **5**, (1998).
 19. Rosencwaig, A., Opsal, J., Smith, W. L. & Willenborg, D. L. Detection of thermal waves through optical reflectance. *Appl. Phys. Lett.* **46**, 1013–1015 (1985).
 20. Tessier, G., Holé, S. & Fournier, D. Quantitative thermal imaging by synchronous thermorefectance with optimized illumination wavelengths. *Appl. Phys. Lett.* **78**, 2267–2269 (2001).
 21. Boccara, A. C., Fournier, D. & Badoz, J. Thermo-optical spectroscopy: Detection by the ‘mirage effect’. *Appl. Phys. Lett.* **36**, 130–132 (1980).
 22. Berto, P. *et al.* Quantitative absorption spectroscopy of nano-objects. *Phys. Rev. B - Condens. Matter Mater. Phys.* **86**, (2012).
 23. Boyer, D., Tamarat, P., Maali, A., Lounis, B. & Orrit, M. Photothermal Imaging of Nanometer-Sized Metal Particles Among Scatterers. *Science (80-.).* **297**, 1160 (2002).
 24. Gaiduk, A., Yorulmaz, M., Ruijgrok, P. V & Orrit, M. Room-Temperature Detection of a Single Molecule’s Absorption by Photothermal Contrast. *Science (80-.).* **330**, 353–356 (2010).
 25. Donner, J. S., Morales-Dalmau, J., Alda, I., Marty, R. & Quidant, R. Fast and transparent adaptive lens based on plasmonic heating. *ACS Photonics* **2**, 355–360 (2015).
 26. Beeckman, J. *et al.* Multi-electrode tunable liquid crystal lenses with one lithography step. *Opt. Lett.* **43**, 271–274 (2018).
 27. Algorri, J. F. *et al.* Tunable liquid crystal multifocal microlens array. *Sci. Rep.* **7**, 17318 (2017).
 28. Li, G. *et al.* Switchable electro-optic diffractive lens with high efficiency for ophthalmic applications. *Proc. Natl. Acad. Sci. U. S. A.* **103**, 6100–4 (2006).

29. Baffou, G. *et al.* Thermal imaging of nanostructures by quantitative optical phase analysis. *ACS Nano* **6**, 2452–2458 (2012).
30. Bon, P. *et al.* Three-dimensional temperature imaging around a gold microwire. *Appl. Phys. Lett.* **102**, 3–6 (2013).
31. Radhakrishnan, T. S. Thermal degradation of poly(dimethylsilylene) and poly(tetramethyldisilylene-co-styrene). *J. Appl. Polym. Sci.* **99**, 2679–2686 (2006).
32. Markos, C., Vlachos, K. & Kakarantzas, G. Thermo-optic effect of an index guiding photonic crystal fiber with elastomer inclusions. in **7753**, 775340 (2011).
33. Holland, J. H. *Adaptation in Natural and Artificial Systems*,. *Ph.D thesis, University of Michigan Press. Ann Arbor, MI.* (1975).
34. Michalewicz, Z. Genetic algorithms+ data structures= evolution programs. (2013).
35. Xu, J. & Zhuang, S. Measurement of lens focal length with Hartmann-Shack wavefront sensor based on 4F system. *Optik (Stuttg)*. **126**, 1303–1306 (2015).
36. Yang, W. *et al.* Simultaneous Multi-plane Imaging of Neural Circuits. *Neuron* **89**, (2016).
37. Hernandez, O. *et al.* Three-dimensional spatiotemporal focusing of holographic patterns. *Nat. Commun.* **7**, 1–10 (2016).
38. Berto, P., Mohamed, M. S. A., Rigneault, H. & Baffou, G. Time-harmonic optical heating of plasmonic nanoparticles. *Phys. Rev. B - Condens. Matter Mater. Phys.* **90**, 1–12 (2014).
39. Jesacher, A., Bernet, S. & Ritsch-Marte, M. Colour hologram projection with an SLM by exploiting its full phase modulation range. *Opt. Express* **22**, 20530–20541 (2014).
40. Harm, W., Jesacher, A., Thalhammer, G., Bernet, S. & Ritsch-Marte, M. How to use a phase-only spatial light modulator as a color display. *Opt. Lett.* **40**, 581 (2015).
41. Yang, W. & Yuste, R. In vivo imaging of neural activity. *Nat. Methods* **14**, 349–359 (2017).
42. Conchello, J. A. & Lichtman, J. W. Optical sectioning microscopy. *Nat. Methods* **2**, 920–931 (2005).
43. Shack, R. V & Platt, B. C. Production and use of a lenticular hartmann screen. *Program. 1971 spring Meet. Opt. Soc. Am. (abstracts only Receiv.* **61**, 15 (1971).
44. Levoy, M., Ng, R., Adams, A., Footer, M. & Horowitz, M. Light field microscopy. *ACM SIGGRAPH 2006 Pap. - SIGGRAPH '06* 924 (2006). doi:10.1145/1179352.1141976
45. Born, Max; Wolf, E. *Principles of Optics. Optics & Laser Technology* **32**, (2000).
46. Lakshminarayanan, V. & Fleck, A. Zernike polynomials: A guide. *J. Mod. Opt.* **58**, 545–561 (2011).